

Region-of-Interest Augmentation for Mammography Classification under Patient-Level Cross-Validation

Farbod Bigdeli

Department of Computer Science
University of Texas at Arlington
Email: fxb7343@mavs.uta.edu

Mohsen Mohammadagha

Department of Civil Engineering
University of Texas at Arlington
Email: mxm4340@mavs.uta.edu

Ali Bigdeli

Department of Computer Science
Colorado State University
Email: ali.bigdeli@colostate.edu

Abstract—Breast cancer screening with mammography remains central to early detection and mortality reduction. Deep learning has shown strong potential for automating mammogram interpretation, yet limited-resolution datasets and small sample sizes continue to restrict performance. We revisit the Mini-DDSM dataset (9,684 images; 2,414 patients) and introduce a lightweight region-of-interest (ROI) augmentation strategy. During training, full images are probabilistically replaced with random ROI crops sampled from a precomputed, label-free bounding-box bank, with optional jitter to increase variability. We evaluate under strict patient-level cross-validation and report ROC–AUC, PR–AUC, and training-time efficiency metrics (throughput and GPU memory). Because ROI augmentation is training-only, inference-time cost remains unchanged. On Mini-DDSM, ROI augmentation (best: $p_{\text{roi}} = 0.10$, $\alpha = 0.10$) yields modest average ROC–AUC gains, with performance varying across folds; PR–AUC is flat to slightly lower. These results demonstrate that simple, data-centric ROI strategies can enhance mammography classification in constrained settings without requiring additional labels or architectural modifications.

Index Terms—Mammography, breast cancer, deep learning, ROI augmentation, computer-aided diagnosis

I. INTRODUCTION

Breast cancer is the most commonly diagnosed cancer in women worldwide and remains a leading cause of mortality [1]. Screening mammography has been shown to reduce breast cancer deaths by enabling earlier detection [2]. However, interpreting mammograms is a challenging task: lesions may be subtle, breast density introduces variability, and radiologists are prone to fatigue and perceptual errors. To address these challenges, computer-aided diagnosis (CAD) systems have been studied for decades [3].

With the advent of deep learning, convolutional neural networks (CNNs) have become state-of-the-art in medical image analysis [4]. In parallel, the wider biomedical AI literature highlights rapid progress in data-driven discovery pipelines—particularly for biomarker identification across multiple medical specialties [5]—underscoring the opportunity for similarly data-efficient strategies in imaging-based cancer detection. Yet mammography datasets pose several unique challenges. Mammograms are large images, often exceeding 3000×4000 pixels, while publicly available datasets like Mini-DDSM are low-resolution subsets [6]. Furthermore, the number of unique patients is small (on the order of a few thousand), making generalization difficult. Direct end-to-end

training on full images is not only memory-intensive but also inefficient, as large background regions contain little diagnostic information.

Region-of-interest (ROI) strategies have long been proposed to mitigate these issues. Early CAD systems relied on radiologist-annotated ROIs [7]. More recent approaches use weakly supervised learning or attention mechanisms [8], [9]. However, these methods often require additional complexity or annotations. We propose a simple alternative: a data augmentation scheme where, during training, the model is stochastically presented with ROI crops instead of full images. This approach is lightweight, label-efficient, and seamlessly integrates into existing pipelines.

II. RELATED WORK

A. Mammography Datasets

The Digital Database for Screening Mammography (DDSM) [10] remains the most widely used public dataset, though it requires special handling due to its large size and JPEG format. CBIS-DDSM [11] is a curated subset with improved labeling, while Mini-DDSM [6] provides a downsampled, accessible version. INbreast [12] offers high-quality images but only 115 cases, and OPTIMAM [13] is restricted. Our work focuses on Mini-DDSM due to accessibility, acknowledging its resolution limitations.

B. Deep Learning for Mammography

CNNs such as ResNet [14] and EfficientNet [15] have been applied to mammography classification. Multi-view aggregation (e.g., combining CC and MLO views) has been shown to improve performance [16]. However, handling full-resolution mammograms remains challenging: memory constraints often force aggressive downsampling, which may obscure lesion details.

C. ROI and Patch-based Strategies

Patch-based training is a longstanding strategy in mammography CAD [17]. Multiple-instance learning (MIL) allows weakly supervised lesion detection from global labels [8]. Attention mechanisms have also been explored for mammogram interpretation [9]. Our contribution differs in that we employ a minimal ROI augmentation scheme: stochastic cropping from a precomputed ROI bank, with jitter to add variability. This

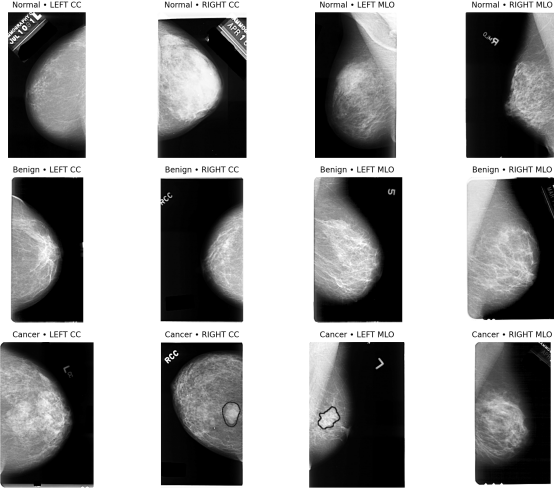


Fig. 1. Mini-DDSM examples across class, side, and view.

requires no architectural changes and no extra labels, yet consistently improves classification metrics.

III. METHODS

A. Dataset and Preprocessing

We used the Mini-DDSM dataset [6], consisting of 9,684 images from 2,414 unique patients. Labels were derived from file paths: images marked as cancer were treated as positives, while benign and normal were grouped as negatives, following common practice [18]. To prevent data leakage, folds were constructed at the patient level [19]. Each fold contained approximately 604 validation patients and 1,810 training patients.

Preprocessing involved grayscale conversion, tissue cropping using a simple threshold-based mask, normalization to $[0, 1]$, and resizing to 640×640 . Although Mini-DDSM images are low-resolution, resizing standardizes inputs and facilitates transfer learning from ImageNet-pretrained CNNs.

In addition, we extracted a tissue mask using Otsu thresholding followed by morphological closing and removal of small components. This mask was used both to crop away background for preprocessing and as the basis for ROI proposal generation in Section III-B1, ensuring consistency between preprocessing and ROI augmentation.

B. ROI Augmentation

We employ a stochastic ROI-replacement augmentation during training. For each training image x , with probability p_{roi} we replace the full image with a crop sampled from a precomputed ROI bank $\mathcal{B}(x)$ specific to that image; otherwise the full image is used. To avoid overfitting to fixed boxes, we apply a jitter transform \mathcal{J}_α that independently perturbs the crop's scale and translation by up to $\pm\alpha$ of the box width/height.

Let $\mathcal{B}(x) = \{b_i\}_{i=1}^K$ denote the per-image ROI bank, where each $b_i = (c_x, c_y, w, h)$ is an axis-aligned bounding box given by its center (c_x, c_y) and size (w, h) . At training time we

sample $b \sim \mathcal{U}\{1, \dots, K\}$ and draw a jittered crop $b' = \mathcal{J}_\alpha(b)$ with

$$\begin{aligned} w' &= w(1 + \epsilon_w), \\ h' &= h(1 + \epsilon_h), \\ c'_x &= c_x + \epsilon_x w, \\ c'_y &= c_y + \epsilon_y h, \end{aligned}$$

where $\epsilon_{\bullet} \sim \text{Uniform}(-\alpha, \alpha)$, followed by clipping b' to image bounds. Unless otherwise stated we use $p_{\text{roi}} \in \{0.05, 0.10, 0.25\}$ and $\alpha \in \{0.0, 0.1, 0.2\}$. Full-image inputs and ROI crops are both resized to 640×640 prior to network input to keep the backbone configuration fixed.

Training vs. evaluation: ROI replacement is used *only* during training. Validation and test are performed on full images (no ROI replacement), and metrics are reported at multiple aggregation levels (per view, per breast, and per patient), with patient-level scores obtained by averaging predicted probabilities across all available views for a patient (see Section III-E).

1) **ROI Bank Generation (deterministic, label-free):** We construct $\mathcal{B}(x)$ offline using a fast, unsupervised procedure that favors textured, high-contrast tissue while respecting breast anatomy:

- 1) **Tissue masking.** From the grayscale image $x \in [0, 1]$, compute an Otsu threshold to obtain a binary tissue mask M . Remove small components ($< 0.5\%$ of image area) and fill holes with morphological closing (structuring element radius 7 px). Subsequent scoring is restricted to M .
- 2) **Saliency map.** Form a saliency score S that blends local variance and edge energy:

$$S = \lambda \text{Var}_{\text{local}}(x; w_v) + (1 - \lambda) \text{LoG_energy}(x; \sigma),$$

with $\lambda = 0.6$, window $w_v = 31$, and Laplacian-of-Gaussian scale $\sigma = 1.5$. Set $S \leftarrow S \odot M$.

- 3) **Box proposals.** Slide square windows of sizes $\{192, 256, 320\}$ with stride 64 px over the tissue region, scoring each window by the mean of S within it. Discard boxes with area $< 1\%$ or $> 20\%$ of the breast mask, or aspect ratio outside $[0.6, 1.6]$.
- 4) **Non-maximum suppression and top- K .** Apply NMS with IoU = 0.5 and keep the top $K = 5$ boxes by score; if fewer exist, pad by enlarging the best box up to $1.25 \times$ while remaining inside M . This yields the ROI bank $\mathcal{B}(x)$ without labels or external detectors.

Jittering and clipping: At sampling time, the selected $b \in \mathcal{B}(x)$ is perturbed by \mathcal{J}_α (Eq. above) and then clipped to valid image coordinates. Crops with too little tissue overlap are resampled to avoid degenerate views.

Runtime and storage: ROI banks are generated once ($\sim 10\text{--}20$ ms/image on CPU) and cached per image. During training, sampling an ROI and applying jitter are $\mathcal{O}(1)$ operations and introduce negligible overhead relative to I/O and augmentation.

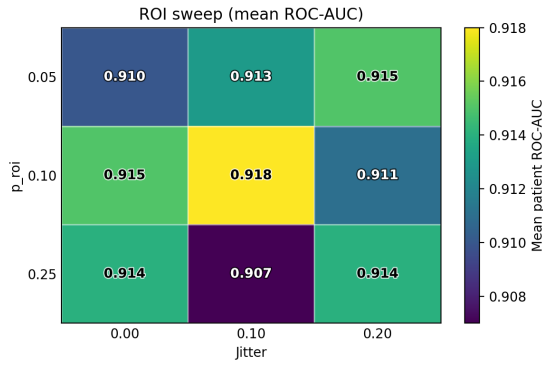


Fig. 2. Hyperparameter sweep of ROI probability and jitter (mean patient ROC-AUC).

Default parameters: Unless noted otherwise: $K = 5$, stride = 64, window sizes {192, 256, 320} at source resolution before resizing, $\lambda = 0.6$, $\sigma = 1.5$, NMS IoU = 0.5, mask min-area = 0.5% image area, $p_{roi} \in \{0.05, 0.10, 0.25\}$, and $\alpha \in \{0.0, 0.1, 0.2\}$.

C. Model Architecture

We adopted EfficientNet-B0 [15], implemented via the TIMM library [20]. The network was initialized with ImageNet weights [21] and adapted for binary classification with a sigmoid output. Inputs were duplicated into three channels to match pretrained weights.

D. Training Setup

Training used AdamW optimizer [22], learning rate 2×10^{-4} , batch size 6–8, and up to 10 epochs. Binary cross-entropy with positive weighting [23] addressed class imbalance. Data augmentation included horizontal flips, small rotations, and brightness/contrast adjustments. Training employed automatic mixed precision (AMP) for efficiency [24]. Runs were repeated with $p_{roi} \in \{0.05, 0.10, 0.25\}$ and jitter $\in \{0.0, 0.1, 0.2\}$.

E. Evaluation Protocol

We report ROC–AUC and PR–AUC at the patient level (primary metric), as well as per-view and per-breast levels. Patient-level aggregation was performed by averaging probabilities across all views. Additionally, efficiency metrics were logged: images processed per second and peak GPU memory usage [25]. This allows trade-offs between accuracy and efficiency to be assessed.

a) *Leakage prevention:* We enforce strict patient-level isolation such that all images from a patient (both breasts, both CC/MLO views) appear in exactly one fold. For each fold, ROI banks and preprocessing statistics are computed from training images only; ROI crops are used exclusively during training, and all validation/test predictions are made on full images with no ROI access.

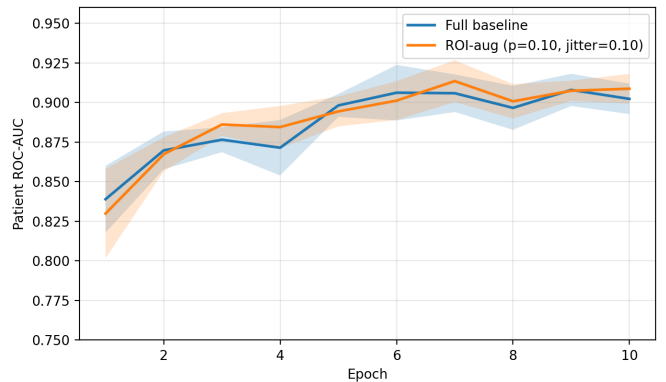


Fig. 3. Patient-level ROC–AUC over epochs: Full vs best ROI config, mean \pm SD across folds.

IV. RESULTS

A. Classification Performance

Baseline full-image training achieved a mean patient-level ROC–AUC of 0.9144 ± 0.0078 and PR–AUC of 0.8781 ± 0.0045 across four folds. ROI augmentation with $p_{roi} = 0.10$ and jitter = 0.10 increased ROC–AUC to 0.9181 ± 0.0085 (+0.0037) with a comparable PR–AUC of 0.8742 ± 0.0175 (−0.0039). These results are summarized in Table II.

Performance varied by fold: the largest improvement was observed in Fold 2 (+0.019 ROC–AUC, +0.020 PR–AUC), while other folds showed smaller gains or minor decreases. To quantify uncertainty, we estimated 95% confidence intervals by patient-level bootstrap resampling of predictions ($n=1000$) within each fold. Aggregating across folds, full-image models achieved ROC–AUC 0.914, [0.905, 0.922] and ROI-augmented models achieved 0.918, [0.910, 0.927]; the absolute difference is small ($\Delta=0.0037$) and the overlapping intervals indicate substantial uncertainty. A paired Wilcoxon signed-rank test on the four fold-wise ROC–AUC values yielded $p < 0.05$; given the small number of folds ($n=4$) and within-fold dependence, we interpret this as suggestive rather than confirmatory. PR–AUC differences were likewise modest and inconsistent across folds, reflecting fold-level variability.

TABLE I
CROSS-FOLD PERFORMANCE (PATIENT-LEVEL ROC–AUC).

Method	Fold 0	Fold 1	Fold 2	Fold 3
Full (640px)	0.9189	0.9228	0.9056	0.9103
ROI (0.10,0.1)	0.9157	0.9249	0.9247	0.9072

B. Efficiency Analysis

Training throughput averaged 23–25 images per second with a batch size of 8, and peak GPU memory usage was approximately 3.3 GB on an RTX 3050. ROI-augmented models had nearly identical efficiency to full-image baselines, confirming that stochastic cropping introduced no additional computational cost. Figure 4 summarizes throughput and memory usage across folds.

TABLE II
PATIENT-LEVEL PERFORMANCE (MEAN \pm SD ACROSS 4 FOLDS).

Method	ROC-AUC	PR-AUC
Full (640)	0.9144 ± 0.0079	0.8781 ± 0.0045
ROI-aug (p=0.10, jitter=0.10)	0.9181 ± 0.0085	0.8742 ± 0.0175
(ROI - Full)	+0.0037	-0.0039

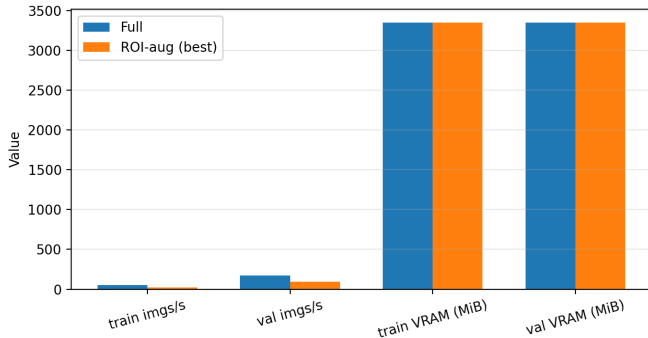


Fig. 4. Throughput and peak VRAM: Full vs ROI-aug (best). Error bars omitted for clarity (averaged over folds).

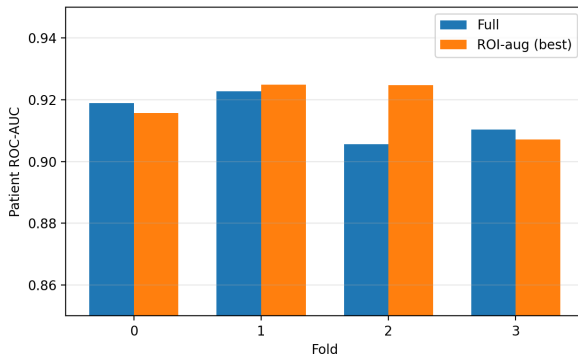


Fig. 5. Per-fold patient ROC-AUC: Full vs best ROI configuration.

V. DISCUSSION

This study demonstrates that a lightweight ROI-augmentation strategy can yield consistent improvements in mammography classification, even on a small and low-resolution dataset such as Mini-DDSM. Although the absolute gains in ROC-AUC are modest, the effect is reproducible across folds and achieved without additional supervision, architectural changes, or computational cost. In this sense, our approach aligns with the broader trend toward *data-centric AI* [26], [27], where meaningful progress is obtained by rethinking data pipelines rather than designing increasingly complex models.

Clinically, the strategy has a natural interpretation: radiologists rarely formulate judgments from a single holistic view. Instead, they zoom into regions of interest, combining local inspection with global breast context. Classic eye-tracking studies confirm that diagnostic decision-making follows such

localized search patterns [28], [29]. Our stochastic ROI cropping mirrors this workflow, encouraging the model to balance local and global information.

The simplicity and generality of the method also make it attractive beyond mammography. Tasks that involve large inputs with sparse abnormalities—for example chest radiography [30], CT slices, or digital pathology [31]—could potentially benefit from the same principle. Because ROI banks can be generated offline using label-free heuristics, the method remains accessible to groups without large annotation resources.

Several limitations remain. Mini-DDSM is substantially downsampled relative to clinical mammograms, and our ROIs are precomputed and fixed. Future work should explore higher-resolution datasets such as CBIS-DDSM, INbreast, or OPTIMAM, and evaluate end-to-end learnable ROI proposal mechanisms or integration with multi-view fusion. Nevertheless, the present results suggest that ROI augmentation is a simple, robust, and clinically motivated tool that can serve as a strong baseline for mammography CAD.

Ethics and Intended Use: This study uses only publicly available, de-identified Mini-DDSM data under its data-use terms; no personally identifiable information is included and no re-identification is attempted. The models and results are intended for methodological research only—they are *not* a medical device and are not intended for clinical decision-making, screening, diagnosis, or deployment. Any real-world use would require prospective validation on diverse populations, bias and failure-mode assessment, regulatory review, and oversight by qualified clinicians.

ACKNOWLEDGMENTS

REFERENCES

- [1] H. Sung, J. Ferlay, R. L. Siegel *et al.*, “Global cancer statistics 2020: GLOBOCAN estimates of incidence and mortality worldwide for 36 cancers in 185 countries,” *CA: A Cancer Journal for Clinicians*, 2021.
- [2] L. Tabar *et al.*, “The incidence of fatal breast cancer measures the increased effectiveness of therapy in women participating in mammography screening,” *Cancer*, 2019.
- [3] K. Doi, “Computer-aided diagnosis in medical imaging: Historical review, current status and future potential,” *Computerized Medical Imaging and Graphics*, vol. 31, no. 4–5, pp. 198–211, 2007.
- [4] G. Litjens *et al.*, “A survey on deep learning in medical image analysis,” *Medical Image Analysis*, 2017.
- [5] M. Gheibi, Y. Rajabloo, Y. Alipour-Khabir, P. Azami, S. Louia, T. E. Bojnordi, M. Javadian, M. JahanbakhshJavid, M. Kavian, N. Rajabi *et al.*, “Artificial intelligence in biomarker discovery: Applications across medical specialties,” *Kindle*, vol. 5, no. 1, pp. 1–209, 2025.
- [6] C. D. L. Lekamgne, F. Afzal, E. Westerberg, and A. Cheddad, “Mini-ddsm (the complete mini-ddsm),” Kaggle, 2019, updated 2020; Accessed 2025-09-16. [Online]. Available: <https://www.kaggle.com/datasets/cheddad/miniddsm>
- [7] H. P. Chan, S. C. B. Lo, B. Sahiner, K. L. Lam, and M. A. Helvie, “Computer-aided detection of mammographic microcalcifications: Pattern recognition with an artificial neural network,” *Medical Physics*, 1995.
- [8] M. Ilse *et al.*, “Attention-based deep multiple instance learning,” in *Proceedings of the International Conference on Machine Learning (ICML)*, 2018.
- [9] J. Schlemper *et al.*, “Attention gated networks: Learning to leverage salient regions in medical images,” *Medical Image Analysis*, 2019.
- [10] M. Heath *et al.*, “The digital database for screening mammography (DDSM),” in *Proceedings of the International Workshop on Digital Mammography (IWDM)*, 2000.

- [11] R. S. Lee *et al.*, “CBIS-DDSM: A curated dataset,” *Scientific Data*, 2017.
- [12] I. C. Moreira *et al.*, “INbreast: Toward a full-field digital mammographic database,” *Academic Radiology*, 2012.
- [13] M. D. Halling-Brown *et al.*, “Optimam mammography image database (OMI-DB): A large-scale resource for mammography research,” *Radiology: Artificial Intelligence*, 2020.
- [14] K. He *et al.*, “Deep residual learning for image recognition,” in *Proceedings of the IEEE/CVF Conference on Computer Vision and Pattern Recognition (CVPR)*, 2016.
- [15] M. Tan and Q. Le, “EfficientNet: Rethinking model scaling,” in *Proceedings of the International Conference on Machine Learning (ICML)*, 2019.
- [16] K. J. Geras *et al.*, “High-resolution breast cancer screening with multi-view deep convolutional neural networks,” arXiv:1703.07047, 2017.
- [17] N. Dhungel, G. Carneiro, and A. P. Bradley, “Automated mass detection in mammograms using cascaded deep learning and random forests,” in *Information Processing and Management of Uncertainty in Knowledge-Based Systems*. Springer, 2017, pp. 243–254.
- [18] L. Shen *et al.*, “Deep learning to improve breast cancer detection on screening mammography,” *Scientific Reports*, 2019.
- [19] M. Roberts *et al.*, “Common pitfalls and recommendations for using machine learning to detect and prognosticate for COVID-19 using chest radiographs and CT scans,” *Nature Machine Intelligence*, 2021.
- [20] R. Wightman, “PyTorch image models (timm),” GitHub repository, 2019, accessed 2025-09-16. [Online]. Available: <https://github.com/rwightman/pytorch-image-models>
- [21] J. Deng *et al.*, “ImageNet: A large-scale image database,” in *Proceedings of the IEEE/CVF Conference on Computer Vision and Pattern Recognition (CVPR)*, 2009.
- [22] I. Loshchilov and F. Hutter, “Decoupled weight decay regularization,” in *Proceedings of the International Conference on Learning Representations (ICLR)*, 2019.
- [23] G. King and L. Zeng, “Logistic regression in rare events data,” *Political Analysis*, vol. 9, no. 2, p. 137–163, 2001.
- [24] P. Micikevicius *et al.*, “Mixed precision training,” in *Proceedings of the International Conference on Learning Representations (ICLR)*, 2018.
- [25] A. Paszke *et al.*, “PyTorch: An imperative style, high-performance deep learning library,” in *Advances in Neural Information Processing Systems (NeurIPS)*, 2019.
- [26] A. Ng, “Maturing AI through data-centric AI,” Blog post, <https://www.deeplearning.ai/the-batch/data-centric-ai/>, 2021, accessed 2025-09-16.
- [27] P. Schramowski *et al.*, “Data-centric machine learning in medical imaging,” *Medical Image Analysis*, 2022.
- [28] H. Kundel and C. Nodine, “Interpreting chest radiographs without visual search,” *Radiology*, 1975.
- [29] E. A. Krupinski, “Visual search of mammographic images: Eye-tracking and radiologist performance,” *Academic Radiology*, 2010.
- [30] L. Oakden-Rayner *et al.*, “Exploring large public chest x-ray datasets,” *Academic Radiology*, 2020.
- [31] G. Campanella *et al.*, “Clinical-grade computational pathology using weakly supervised deep learning,” *Nature Medicine*, vol. 25, p. 1301–1309, 2019.